Stepwise Deep Feature Transfer Model for Martian Landform Mapping with Small Number of Labeled Samples

Hui Zhao, Sicong Liu, *Senior Member, IEEE,* Xiaohua Tong, *Fellow, IEEE*, Qian Du, *Fellow, IEEE*, Lorenzo Bruzzone, *Fellow, IEEE,* Huan Xie, *Senior Member, IEEE*, Yongjiu Feng, Kecheng Du, Jie Zhang, Yonggang Xiong

***Abstract*—The Martian surface landforms are highly related to the safe landing and traversability of Mars rovers. Furthermore, landforms associated with the presence of water/ice, minerals and biosignatures can provide valuable insights for Mars exploration missions, particularly in relation to the selection of landing or sample collection sites. The small number of Martian landform datasets and the scarcity of labelable landform samples over Mars make the precise mapping of Martian landforms a challenging task. In this article, we propose a stepwise deep feature transfer (SDFT) model for the mapping of Martian landforms with a small number of labeled samples. The SDFT model comprises two transfer steps. In the first transfer step, a deep learning model trained on a large public source dataset from Earth is transferred to a medium sized public dataset from Mars. This transfer is conducted through a standard pre-training and fine-tuning procedure utilizing a linear classifier. In the second transfer step, the model is further transferred to a small number of target datasets on Mars through a pre-training and fine-tuning procedure with a cosine distance classifier. The stepwise training technique mitigates the challenges associated with varying datasets and small training samples. The proposed SDFT model has been validated on two self-built sample sets using images from the Mars Reconnaissance Orbiter's Context Camera (CTX). It has also been employed for landform mapping in two local regions with small samples to evaluate its effectiveness in comparison with existing state-of-the-art methods.**

***Index Terms*—Mars exploration, Martian landform, Fine mapping, Feature transfer, CTX images, small number of samples.**

This work was supported in part by the National Natural Science Foundation of China under Grants 42241130, 42221002, in part by the Shanghai Rising-Star Program (21QA1409100), and the Fundamental Research Funds for the Central Universities. (*Corresponding author: Sicong Liu*)

Sicong Liu, Xiaohua Tong, Huan Xie, Yongjiu Feng, Kecheng Du, Jie Zhang and Yonggang Xiong are with the College of Surveying and Geoinformatics, Tongji University, Shanghai 200092, China (e-mail: sicong.liu@tongji.edu.cn; xhtong@tongji.edu.cn; huanxie@tongji.edu.cn, yjfeng@tongji.edu.cn, kecheng_du@tongji.edu.cn; zhangjie22@tongji.edu.cn; ygxiong@tongji.edu.cn).

Hui Zhao was with the College of Surveying and Geoinformatics, Tongji University, Shanghai 200092, China, and is now with School of Spatial Information and Geomatics Engineering, Anhui University of Science and Technology, Huainan 232001, China (e-mail: zhaohui@aust.edu.cn)

Qian Du is with the Department of Electrical and Computer Engineering, Mississippi State University, Starkville, MS 39762, USA (e-mail: du@ece.msstate.edu).

Lorenzo Bruzzone is with the Department of Information Engineering and Computer Science, University of Trento, I-38123, Italy (e-mail: lorenzo.bruzzone@unitn.it).

I. Introduction

Mars is the Earth-like planet in the solar system with the greatest potential for harboring life. It is also the current hotspot for international deep space exploration. The Mars exploration missions conducted by numerous countries and organizations have generated substantial data about the planet, including information collected by Orbiters and Rovers [1-3]. The commonly used Martian orbiter data include MOLA (Mars Global Surveyor's Mars Orbiter Laser Altimeter) [4], the global Martian digital elevation model (DEM) data derived from it, THEMIS (Mars Odyssey Orbiter's Thermal Emission Imaging System) [5] and CTX (Mars Reconnaissance Orbiter's Context camera) [6] data that cover almost the entire surface of Mars. Additionally, high-resolution datasets, such as HiRISE (Mars Reconnaissance Orbiter's High Resolution Imaging Science Experiment) [7] and HiRIC (High Resolution Imaging Camera on China's First Mars Exploration Tianwen-1 Mission) [8], provide detailed images of specific regions on Mars. The Mars Reconnaissance Orbiter's Compact Reconnaissance Imaging Spectrometer for Mars (CRISM) has been used in the study of Mars' mineralogy [9]. The extensive data acquired through the ongoing Martian orbiter exploration initiatives facilitate a comprehensive understanding of Mars and enable new discoveries.

It is essential that Martian surface landforms are accurately identified in order to facilitate further scientific exploration of the planet. The study of mud volcanism and the morphology of impact craters in Utopia Planitia on Mars provides evidence for the existence of an ancient ocean [10]. Crater morphometry allows for the inference of the origin, age and surface processes of the floor unit, as well as the deduction of implications for erosion rates and climate change on Mars [11, 12]. Meanwhile, the precise mapping of Martian landforms is essential for specific Mars exploration missions, including the selection of landing sites, the assurance of safe landings, the traversability of Mars rovers, and the collection of samples. Specifically, the slope, roughness and surface load-bearing of different Martian landforms must be taken into account when selecting a landing site [13]. Furthermore, the presence of water/ice, minerals and biosignatures can provide valuable insight into potential landing sites or sample collection locations [14].

In order to obtain the distribution and morphology of Martian landforms, usually a manual visual interpretation is employed, which is generally considered to be a reliable and accurate approach. A new global database of Mars impact craters with a

diameter of at least 1 km, comprising 384,343 entries, was created manually using ArcGIS software based on THEMIS daytime infrared data [15, 16]. Planet Four: Terrains (P4T) is an online citizen science project, where the general public was enlisted to identify and manually label seasonally sculpted terrains in the South Polar region of Mars using CTX images. These terrains include araneiform, Swiss cheese terrain and craters [17, 18]. The Mars Global Digital Dune Database was created to archive the location of large dark dunes on Mars, and the dune field was outlined in a shapefile using Java Mission-Planning and Analysis for Remote Sensing GIS [19]. The terrain features of a 4 × 4 degree area in Southern Utopia Planitia, which contains the landing site of the Zhurong rover from the Chinese Tianwen-1 mission, were mapped in ArcMap using the NASA CTX global image mosaic as the base map to understand the geology of this region [20]. However, the process of sketching Martian landforms is typically time-consuming and is often influenced by the personal knowledge and biases of the researchers involved.

It is therefore necessary to develop an automated Martian landform detection algorithm. In previous studies, the DEM served as the primary data source for extracting multiple terrain attributes, which were then used in unsupervised classification [21-25]. Furthermore, high spatial resolution images were used for identifying dune fields, dark slope streaks, dust devil tracks, and gullies through the extraction of specific features and the implementation of machine learning classification algorithms [26-31]. In recent years, deep-learning-based approaches have also been widely applied to the identification of Martian landforms [32]. However, the volume of data and the maturity of the techniques for identifying Martian surface features are much less advanced than those for Earth observation, presenting a significant challenge for Martian landform classification. In the following section, we distinguish the classification methods for Martian landforms into two categories: those that employ supervised learning, and those that utilize transfer learning.

For the former, SPOC (Soil Property and Object Classification) technique was developed to identify terrain types and features on both orbital and ground-based images. This technique was built based on the DeepLab network and reference ground maps with identified 17 terrain classes by using HiRISE images for eight candidate landing sites of the Mars 2020 Rover mission. These maps were used to analyze the traversability of the terrain [33, 34]. The NOAH-H (Novelty or Anomaly Hunter - HiRISE) terrain classification system was constructed using the DeepLab model to classify HiRISE images covering the Oxia Planum and Mawrth Vallis regions. Fourteen descriptive classes were identified, providing a good indication of the prevalence and distribution of different terrain types [35]. The terrain classification in these tasks can be viewed as a supervised semantic segmentation problem, where a class label is assigned to each pixel in an input image. Pixel-level annotation, which outlines the boundaries of the landform, is necessary for the training of the algorithms. In [35], the high confidence landform regions were annotated in 1,504 128 m × 128 m HiRISE images. However, this process is labor-intensive and requires input from domain experts.

For the transfer learning method, in [36], a convolutional neural network (CNN) based on the VGG-16 architecture with deep transfer learning is employed to automatically classify four groups of Martian rocks. In [37], the AlexNet trained on Earth images from the ImageNet dataset, was adapted via transfer learning to classify images from Mars. These images were downloaded from the Planetary Data System (PDS) Image Atlas, and twenty-four classes from Martian rover images and six classes (*i.e., craters, bright sand dunes, dark sand dunes, dark slope streaks, other and edge*) from HiRISE orbital images were automatically identified to help users to quickly find images of interest. In [38], three new classes (*i.e., impact ejecta, spider, and Swiss cheese*) observed from HiRISE orbital images were incorporated into the above-mentioned dataset by a proper tuning the AlexNet network pre-trained on Earth images. In [37], 3,820 HiRISE images of the Martian surface were labeled, while the new HiRISE dataset in [38] increased the number of labelled images to 10,815. In [39], a novel DoMars16k dataset of CTX images, containing 16,150 samples of 15 landforms commonly found on the Martian surface, was introduced. Furthermore, three neural network training approaches (*i.e.,* from scratch, transfer learning and pre-training) were compared using the widely used CNN architectures (*i.e.*, AlexNet, VGG, ResNet and DenseNet). The optimal combination was then used to map Martian landforms based on a pixel-by-pixel sliding-window approach. The landform classification tasks can be regarded as scene classification problems, whereby a class label is assigned to an input image. Although scene-level annotation of a square image representing a landform category is a more straightforward process than pixel-level annotation, it is still a time-consuming task, particularly when dealing with a large number of samples, especially when employing deep learning classification techniques.

Based on the aforementioned analysis, it is evident that there are important issues in the current literature that require further attention. Firstly, the process of labeling an adequate number of samples (*e.g.*, 1,504, 10,815 and 16,150 samples in [35], [38] and [39], respectively) when utilizing deep learning techniques for Martian landform classification is inherently time-consuming. Furthermore, some landforms in the local target region may be insufficiently represented, making it difficult to label an adequate number of samples. However, when the available public datasets were directly used, they may not be compatible with the specific considered localized target region in terms of landform classes and scale (*e.g.*, [40]). It is therefore necessary to address the challenges of the classification of Martian landforms with a small number of samples. Secondly, the deep learning models that do not use transfer learning (*e.g.*, [33, 35]) require a large number of samples for the training from scratch, that increase with the number of parameters of the network. In the current used deep transfer learning models (*e.g.*,[36-39]), the features trained on the large Earth dataset were transferred to the Mars dataset. However, there are significant differences between the two types of datasets in terms of the classes represented, with the

Earth dataset containing a much greater diversity of classes than that of Mars. Additionally, the images in the Earth dataset typically have at least three bands, while those in the Mars dataset are single-band. These differences highlight the need for further improvements to the single-step transfer process.

To address the aforementioned issues and challenges, this work proposes a stepwise deep feature transfer (SDFT) model for Martian landforms mapping with a small number of labeled samples. Two Martian areas were selected for the construction of the landform datasets: the Southern Utopia Planitia (the Tianwen-1 Zhurong rover landing region) and the Oxia Planum (the prospective ExoMars landing region). The obtained results confirm the effectiveness of the proposed approach. The main contributions of this paper are as follows.

1) A novel SDFT model for Martian landform mapping is proposed, aims to specifically handle small numbers of labeled samples, particularly in specific local target regions where some landforms are insufficiently represented.

2) In addressing the issue of misalignment between the public Earth dataset and the specific Martian target data, the proposed SDFT model incorporates two transfer steps, *i.e.*, Features Transition Transfer (FTT) and Features Adaptation Transfer (FAT). The FTT step involves the standard pre-training and fine-tuning procedure, utilizing a linear classifier, to transfer public source data from Earth (*i.e.*, ImageNet) to Mars (*i.e.*, DoMars16k). This step serves to mitigate the data and class gaps between Earth and Mars, and prepares the features for the subsequent step. In the FAT step, a pre-training and fine-tuning procedure with the cosine distance classifier is used to transfer the deep features from the source data (*i.e.*, DoMars16k) to the target data, thereby adapting to the small number of training samples and enabling more accurate classifications by reducing intra-class variations with a small training set.

3) The SDFT model has the potential to be used for transfer between different resolutions and source datasets, and also provides a new solution for landform classification of Mars and other planets.

The rest of this paper is organized as follows. The proposed approach is described in detail in Section II. Experimental results and analyses are presented in Section III. Finally, Section IV draws the conclusions.

II. Proposed SDFT Approach

The proposed SDFT model aims to map the fine landforms of Martian localized target regions based on a customized landform system and a small amount of labeled samples. Fig. 1 illustrates the overall block diagram of the proposed approach, which primarily consists of three steps: 1) Features Transition Transfer (FTT); 2) Features Adaptation Transfer (FAT); 3) Superpixel-guided Landform Mapping.

In the FTT step, the source data (denoted as source data 1) is the public Earth dataset (*i.e.*, ImageNet [41]) comprising common terrestrial scenes and everyday objects across 1,000 categories (1.2 million images). Although not a specialized landform dataset, it includes Earth scenes (*e.g.*, volcanoes, cliffs, valleys, alps) and everyday objects (*e.g.*, beer bottles, ladybugs, sea lions). This dataset was selected because models trained on its massive scale acquire universal visual features (*e.g.*, edges, textures, shapes) rather than domain-specific landform knowledge. The target data (denoted as source data 2) in the FTT step, which also serves as the source data in the FAT step, is the public Martian dataset (*i.e.*, DoMars16k [39]). It consists of 16,150 images and 15 classes, such as *Aeolian Straight*, *Crater*. Labeled image were selected from across the entire Martian surface. Since the DoMars16k dataset may not align with the specific target region regarding landform classes and scale, the target data for the FAT step was customized based on the actual conditions of the local study region (see in Section III.B). The number of labeled samples is large in source data 1, medium in source data 2, and small in the target data.

The two transfer processes of the proposed SDFT model are shown in Fig. 2. After the FTT step, the transitional features for the FAT step are prepared by reducing the data and class domain gap between Earth and Mars. Furthermore, the FAT step further adapts these features to the small number of target data on Mars. The DenseNet161 is used as the feature extractor f_θ during both training and fine-tuning stages of both FTT and FAT processes. In this context, the dimension of the encoded feature is denoted as d, the source data 1 is represented by X_1, the source data 2 is represented by X_2, the target data is represented by X_3, the number of classes of source data 1, source data 2 and target data are represented by c_1, c_2 and c_3, respectively. x_i, x_j and x_k are used to denote the training samples in the source data 1, source data 2 and target data, respectively.

A. Step 1: Features Transition Transfer (FTT) Step

In the training stage of the FTT step, the feature extractor $f_{\theta 1}$ and classifier $g_{\omega 1}$ are trained from scratch using the large source data on Earth (*i.e.*, ImageNet). The classifier g_ω consists of a linear layer, followed by a softmax function σ. The predicted values of the training stage can be expressed as:

$$\hat{y}_1 = \sigma(W_1^T f_{\theta 1}(x_i)) \tag{1}$$

where $W_1 \in \mathbb{R}^{d \times c_1}$ is the weight matrix of linear layer 1, and $x_i \in X_1$.

The FTT step follows the standard transfer learning procedure of pre-training and fine-tuning. To resolve Earth-Mars domain discrepancies, two strategies were implemented. First, spectral domain adaptation was employed, where single-band CTX images are replicated into three channels to satisfy the input requirements. Second, class alignment was performed by replacing the 1000-class classifier (the linear layer 1) from ImageNet with a 15-node classifier (a new linear layer 2) corresponding to the landform classes in DoMars16k. Furthermore, the pre-trained parameters in the feature extractor $f_{\theta 1}$ are fine-tuned on source data 2, resulting in a new feature extractor $f_{\theta 2}$, and semantic discrepancy between the Earth and Mars domains was mitigated through feature transfer via pre-training and fine-tuning. The model was initially pre-trained on ImageNet to extract universal visual features (*e.g.*, edges, textures, shapes). These features were subsequently fine-tuned on the Martian DoMars16k dataset to

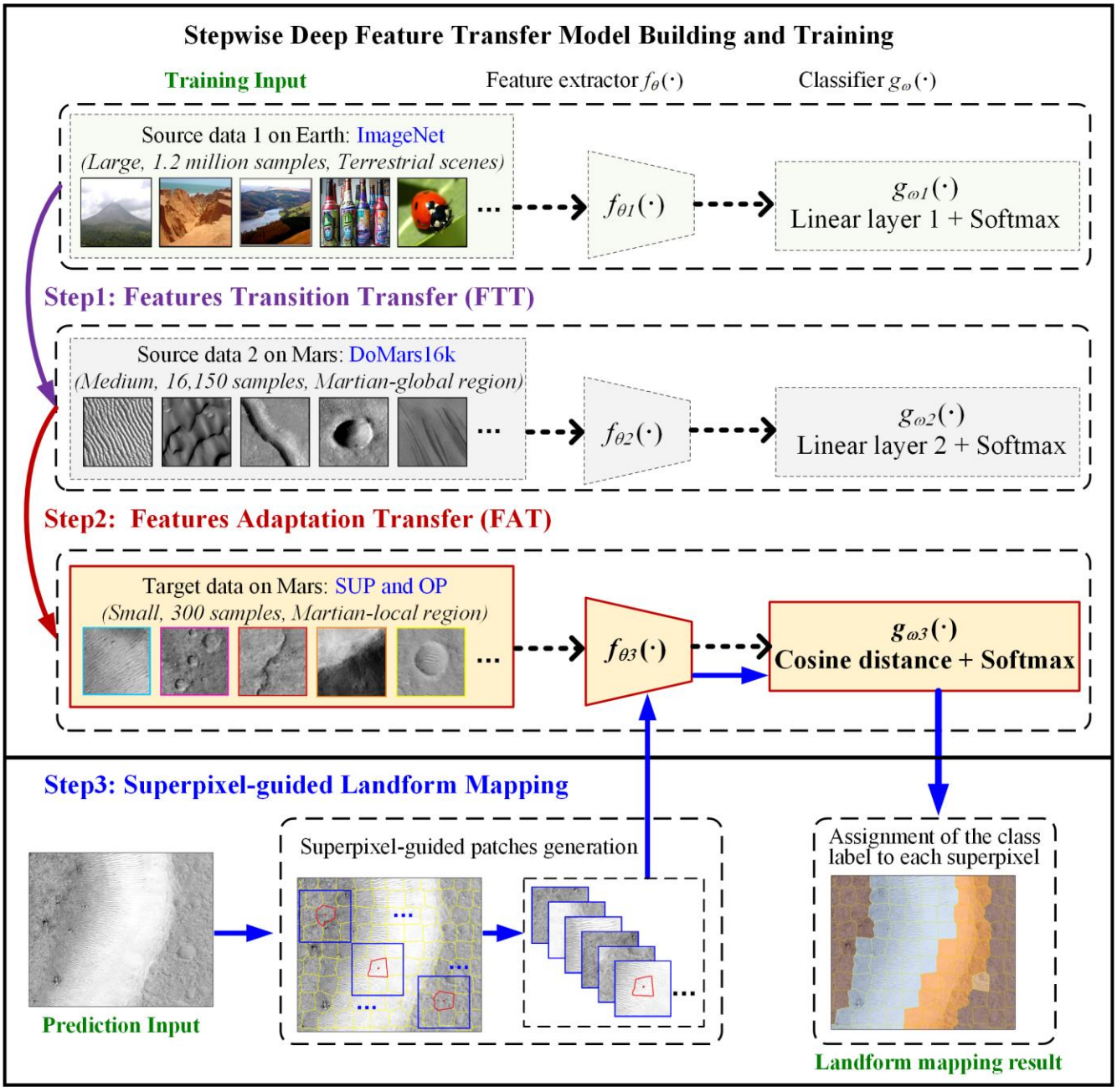

Fig. 1. The block scheme of the proposed approach.

generate domain-specific semantic representations through weight recombination. The two extractors are related by

$$f_{\theta 2} = F(f_{\theta 1}) \tag{2}$$

where F is the operation of feature fine-tuning. The predicted values of the fine-tuning stage 1 can be expressed as:

$$\hat{y}_2 = \sigma(W_2^T f_{\theta 2}(x_j)) \tag{3}$$

where $W_2 \in \mathbb{R}^{d \times c_2}$ is the weight matrix of linear layer 2, and $x_j \in X_2$.

B. Step 2: Features Adaptation Transfer (FAT) Step

In the FAT step, the target data comprises a small number of labelled samples from Martian regions, which present a challenge for training deep learning classifiers. Consequently, the standard deep learning transfer approach of pre-training and fine-tuning used in the FTT step may not yield accurate classification results. The importance of reducing intra-class variations of features has been highlighted in few-shot classification methods, and the concept of distance-based classification has been investigated in [42], with further observation on cosine-similarity for the few-shot classification given in [43]. The experiments in [43] demonstrate that training a cosine-similarity based model outperforms previous state-of-the-art approaches in the few-shot recognition task. Accordingly, we use the cosine-similarity classifier in the FAT step to accommodate the small number of samples. The training procedure of the fine-tuning stage 2 is the same as the fine-tuning stage 1 with the exception of the classifier design. The pre-trained parameters in the feature extractor $f_{\theta 2}$ are

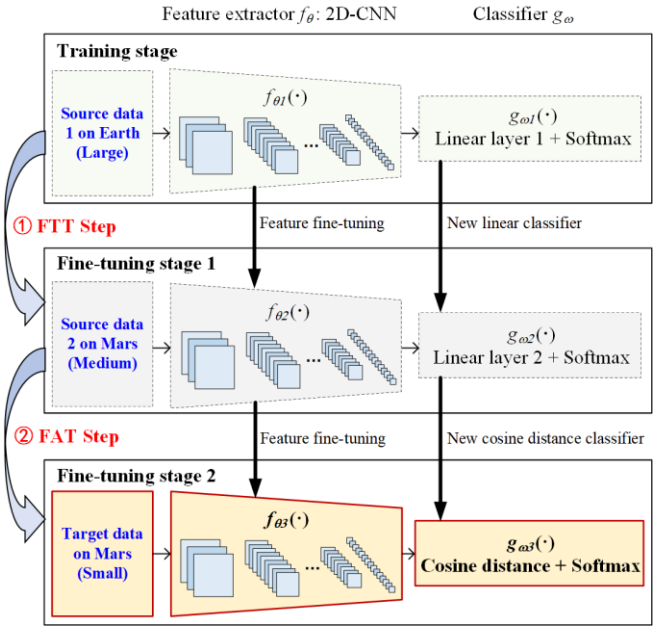

Fig. 2. The flowchart of the proposed SDFT model.

fine-tuned to generate a new feature extractor $f_{\theta 3}$ through the operation of feature fine-tuning F:

$$f_{\theta 3} = F(f_{\theta 2}) \tag{4}$$

where $W_3 \in ¡^{d \times c_3}$ is the weight matrix of the classifier in the fine-tuning stage 2, and $W_3 = [w_1, w_2, \text{K } w_{c_3}]$. For the feature $f_{\theta 3}(x_k)$, its cosine-similarity for each weight vector $[w_1, w_2, \text{K } w_{c_3}]$ is computed and the similarity scores of all classes are calculated as:

$$sim_t = \frac{w_t^T f_{\theta 3}(x_k)}{\|w_t\| \cdot \|f_{\theta 3}(x_k)\|} \tag{5}$$

where $t = 1, 2, \text{K }, c_3$, and $\| \ \|$ stands for the vector norm. The predicted values of the model of fine-tuning stage 2 can be expressed as:

$$\hat{\bar{y}}_3 = \sigma(\tau \cdot sim_t) \tag{6}$$

where τ is a learnable scalar controlling the peakiness of the probability distribution generated by the softmax operator, since the range of cosine similarity is fixed to [-1, 1]. The models in all the three training stages are trained by minimizing a standard cross-entropy classification loss.

C. Step 3: Superpixel-guided Landform Mapping

While the model from fine-tuning 2 requires square patch inputs and outputs patch-level classifications, our objective is landform mapping with clearly delineated landform boundaries, rather than the isolated patch predictions. Therefore, we adopt the superpixel-guided landform mapping method proposed in [40], which workflow is illustrated in Fig. 3.

First, the Simple Linear Iterative Clustering (SLIC) algorithm [44] is used for superpixel segmentation. The resulting superpixel-level segments exhibit accurate local morphological homogeneity and boundary adherence. This can be achieved by carefully tuning the compactness parameter m and superpixel count K in the SLIC operation [40]. Second, the patches are created with the guidance of the superpixels. For a given superpixel segmentation, an $n \times n$ size patch, centered on the superpixel centroid, is created. The size of the created patches is the same as the target samples labeled in Step 1. Subsequently, each patch is then fed into the trained fine-tuning 2 model to estimate the class, and the class value is assigned to the corresponding superpixel.

III. Experimental Results and Discussions

The proposed approach was applied to two manually labelled datasets for quantitative evaluation. A small number of samples from two localized regions of Mars (*i.e.*, Southern Utopia Planitia and Oxia Planum) were labeled to train the model, which was then used for landform mapping. The quantitative and qualitative classification results demonstrate the effectiveness of the proposed SDFT model.

A. Experimental Setup and Parameter Setting

SLIC: Based on multiple trials, the compactness m is set to 0.2, and b is set to 65, and K was empirically defined as:

$$K = (H \times W) / (b \times b) \tag{7}$$

where H and W are the height and weight of the input image, respectively, and b is pre-defined to be close to the size of the interested landform in the sample patches [40].

Model training: The Stochastic Gradient Descent (SGD) optimization is used, with a learning rate of 0.01, a momentum of 0.9, a batch size of 64, and 50 training epochs.

Landform prediction: The training sample size n is equal to 200.

Algorithms were implemented using Python, where the deep learning networks were built using Pytorch. Experiments were carried out on Ubuntu 18.04.5, with Intel Xeon Gold 6130 CPUs at 2.10 GHz, 159 GB of RAM, and an NVIDIA GRID P40-24Q GPU with 22GB of memory.

B. Study area and data

The experiments are performed on two study areas: SUP and OP region. SUP represents the local region contained within the area of Southern Utopia Planitia; OP consists of the regions of Oxia Planum, McLaughlin Crater and Oyama Crater. Fig. 4 illustrates the locations of the two study areas (highlighted in red and blue rectangles) and the coverage of DoMars16k dataset overlaid on the MOLA DEM. Green stars mark the centroids of the 163 CTX images used in generating the DoMars16k dataset. As one can see, there is only one image overlapped with OP. Consequently, the reported accuracy of subsequent transfer experiments was minimally affected by the overlap of study areas. Both the SUP and OP contain a range of 8°×12°). The mosaic CTX images with a resolution of 5 m were used for constructing samples and mapping.

1) Source and target datasets for quantitative analysis

Three datasets (*i.e.*, source data 1, source data 2, and target data) are required when employing the proposed SDFT approach. The source data 1 and source data 2 are publicly

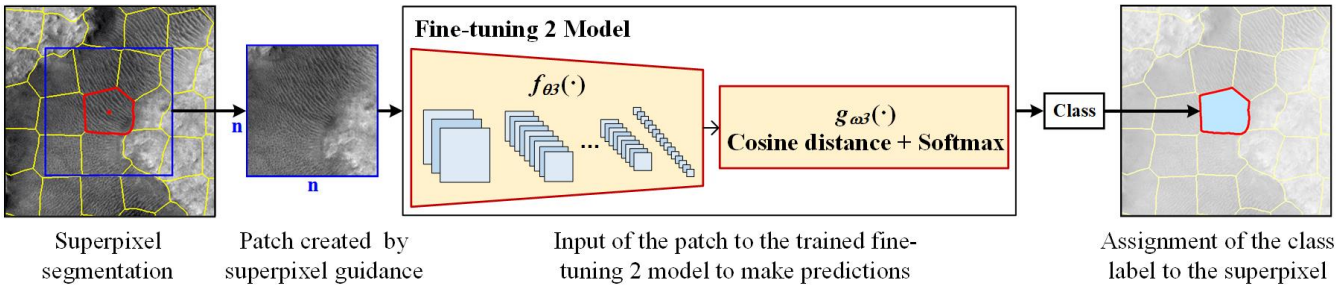

Fig. 3. The flowchart of the superpixel-guided landform mapping.

TABLE I
THE LANDFORM CLASSES CONSIDERED AND EXAMPLE SAMPLES OF SOURCE DATA 2 AND TWO TARGET DATA SETS ON MARS.

		Thematic Groups				
		Genetic Landforms			Morphic Landforms	
Source data 2 on Mars	**DoMars16k (15 classes)**	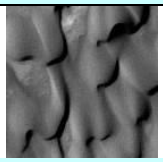 *Aeolian Curved*	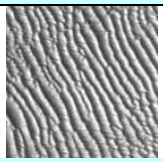 *Aeolian Straight*	 *Crater*	 *Crater Field*	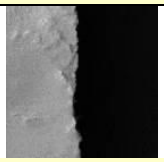 *Cliff*
		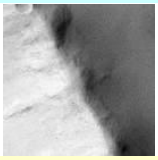 *Ridge*	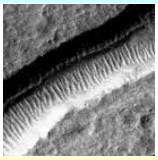 *Channel*	 *Mounds*	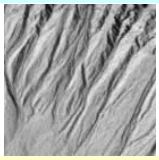 *Gullies*	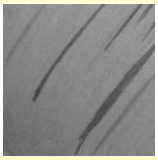 *Slope Streaks*
		 *Mass Wasting*	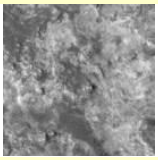 *Mixed Terrain*	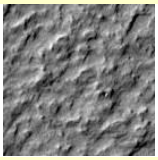 *Rough Terrain*	 *Smooth Terrain*	 *Textured Terrain*
Target data on Mars	**SUP (10 classes)**	 *Crater*	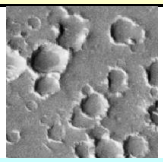 *Crater Field*	 *Cliff*	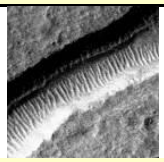 *Channel*	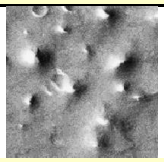 *Mounds*
		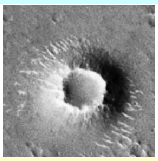 *Pitted Cone*	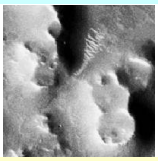 *Pitted Cone Cluster*	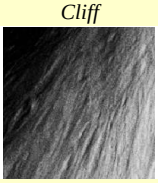 *Crater Wall and Bottom*	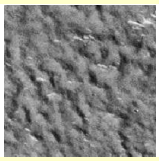 *Rough Terrain*	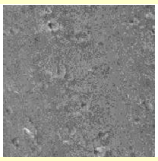 *Smooth Terrain*
	OP (9 classes)	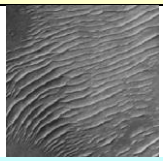 *Aeolian Straight*	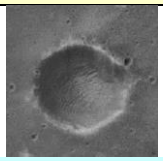 *Crater*	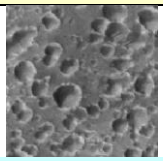 *Crater Field*	 *Cliff*	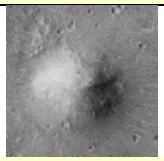 *Mounds*
		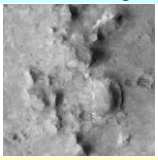 *Rugged Outcrop*	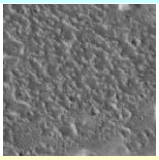 *Rough Terrain*	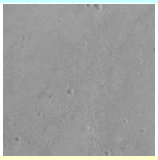 *Smooth Terrain*	 *Textured Terrain*	

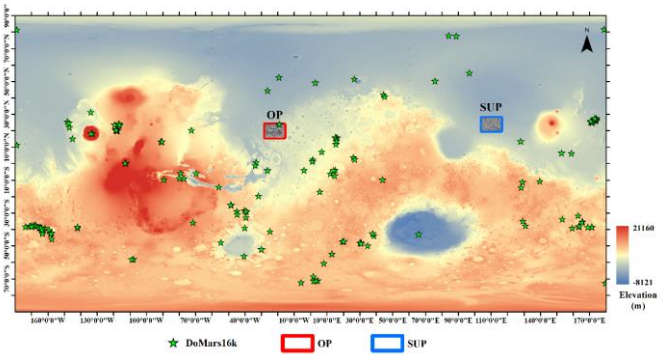

Fig. 4. Location of the two target areas (SUP and OP) and DoMars16k dataset represented on the color-coded MOLA DEM.

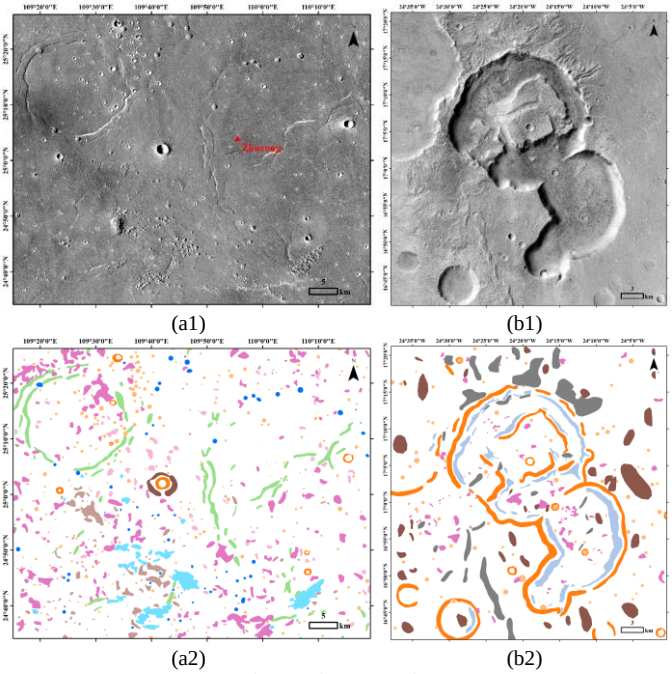

Fig. 5. The CTX images used for landform classification on the two study areas: (a) Local SUP (image size: 12,821 × 10,426 pixels); (b) Local OP (image size: 7,555 × 8,028 pixels). (a2) and (b2) are reference maps to (a1) and (b1), respectively.

TABLE II
THE CONSIDERED LANDFORM CLASSES AND THE NUMBER OF TRAINING SAMPLES ON EACH IMAGE IN THE TWO STUDY AREAS.

Local SUP		Local OP	
Landform Classes	**Number**	**Landform Classes**	**Number**
Crater Rim	15	*Aeolian Straight*	13
Crater Field	15	*Crater Rim*	13
Channel	18	*Crater*	14
Crater	14	*Crater Field*	12
Mounds	12	*Textured Terrain*	21
Pitted Cone	16	*Rough Terrain*	17
Pitted Cone Cluster	18		
Rough Terrain	7		
Smooth Terrain	20		

available, whereas the target data has been manually labeled in accordance with the landform system prevailing in the study area. To assess the effectiveness of the proposed SDFT approach, two target data sets (denoted as SUP and OP) were created based on the SUP and OP region.

TABLE I provides an overview of the landform classes and illustrative samples of the source data 2 (*i.e.*, DoMars16k) and the two target datasets (*i.e.*, SUP and OP) on Mars. DoMars16k dataset comprises two thematic groups with 15 distinct landform classes. It was constructed using images from the Mars Reconnaissance Orbiter's CTX instrument. The SUP and OP datasets contain 10 and 9 classes, respectively. The SUP and OP samples are constructed using mosaic CTX images. Each class in these target datasets includes 300 samples, 100 of which are employed for the training extraction of training samples, while the remaining 200 are used for testing.

As one can see in TABLE II, although the DoMars16k dataset covers relatively comprehensive Martian landform classes, its class distribution diverges significantly from localized target regions. For example, the SUP dataset lacks instances of Aeolian Bedforms, while *Slope Streaks* present in the DoMars16k dataset are absent from both the SUP and OP datasets. Additionally, the scale of the *Mounds* class in the OP region is considerably larger than that of DoMars16k, reflecting significant differences in Martian landform class scales. To refine the landform in the SUP region, we have added the *Pitted Cone* and *Pitted Cone Cluster* classes to the SUP classes relative to DoMars16k. These discrepancies underscore the necessity of customizing the landform classification for target regions.

Note that this study focuses on descriptive landform features rather than interpretative landform units. The morphological divisions employed are highly detailed, particularly for fine-scale classification within local regions. For example, large impact craters are broken down into constituent components such as rims and floors. While precise landform units were not directly derived, these classification results provide foundational data for subsequent landform unit delineation.

2) Study area and samples for mapping

To evaluate the mapping effectiveness of the proposed SDFT model, two local study areas were selected. The first is the local area of Southern Utopia Planitia (denoted as local SUP), which contains the China's Tianwen-1 Zhurong landing site (25.066°N, 109.925°E). The second is the local area near Oxia Planum (denoted as local OP), which is the prospective ESA's ExoMars candidate landing region. Utopia Planitia is the largest recognized circular impact basin in the northern hemisphere of Mars [45]. It was flooded and filled by extensive sedimentary materials from the Vastitas Borealis interior unit [46]. Oxia Planum is a region of low relief located on the southwest margin of Arabia Terra. Its bedrock units are characterized by the presence of hydrous clay [47].

The CTX images and reference maps of the two study areas are shown in Fig. 5. The image sizes in Fig. 5 (a1) and (b1) are 12,821×10,426 and 7,555×8,028 pixels, respectively. As illustrated in TABLE II, the landform systems were developed with nine and six classes for SUP and OP areas, respectively. To evaluate the effectiveness of the proposed SDFT approach for mapping with a small number of samples, some training samples were manually labeled in the two study areas. The number of training samples in the two study areas are presented in TABLE II. It can be observed that the maximum number of

TABLE III
OA (%) OF FINE-TUNING STAGE 1 ON DOMARS16K DATASET.

GoogLeNet	EfficientNet_b0	ResNet18	Inception_v3	DenseNet161
93.09±0.24	93.25±0.45	93.28±0.32	93.66±0.41	94.24±0.24

TABLE IV
OA (%) OF FINE-TUNING STAGE 2 WITH DIFFERENT NUMBER OF TRAINING SAMPLES ON THE SUP DATASET.

Feature Extractors	Number of samples							
	5	10	20	30	40	50	60	70
GoogLeNet	89.96 ±0.32	94.02 ±0.08	96.24 ±0.05	96.74 ±0.08	97.30 ±0.16	97.49 ±0.05	97.28 ±0.58	97.72 ±0.13
EfficientNet_b0	90.37 ±0.38	**94.52** ±0.11	95.92 ±0.08	96.55 ±0.05	97.20 ±0.10	97.36 ±0.08	97.37 ±0.06	97.41 ±0.04
ResNet18	87.53 ±1.10	90.73 ±0.30	95.37 ±0.08	96.70 ±0.13	96.98 ±0.18	97.31 ±0.55	97.47 ±0.15	97.81 ±0.13
Inception_v3	88.78 ±0.73	94.05 ±0.07	95.57 ±0.17	96.25 ±0.41	96.86 ±0.23	97.21 ±0.15	97.34 ±0.13	97.48 ±0.15
DenseNet161	**91.63** ±0.18	94.50 ±0.10	**96.20** ±0.20	**96.71** ±0.52	**97.44** ±0.40	**97.58** ±0.39	**97.78** ±0.14	**97.99** ±0.12

TABLE V
OA (%) OF FINE-TUNING STAGE 2 WITH DIFFERENT NUMBER OF TRAINING SAMPLES ON THE OP DATASET.

Feature Extractors	Number of samples							
	5	10	20	30	40	50	60	70
GoogLeNet	90.93 ±0.40	96.13 ±0.13	97.31 ±0.17	97.64 ±0.18	97.20 ±0.79	98.07 ±0.29	98.30 ±0.40	98.11 ±0.17
EfficientNet_b0	**93.37** ±0.47	96.54 ±0.10	97.39 ±0.24	97.58 ±0.20	**98.36** ±0.16	**98.34** ±0.12	98.36 ±0.08	98.37 ±0.07
ResNet18	91.38 ±0.49	95.03 ±0.12	96.03 ±0.14	96.70 ±0.18	97.14 ±0.31	97.47 ±0.51	97.52 ±0.31	97.86 ±0.21
Inception_v3	90.30 ±0.89	92.62 ±1.25	95.50 ±0.99	96.81 ±0.41	97.71 ±0.27	97.51 ±0.49	98.00 ±0.37	97.76 ±0.55
DenseNet161	92.27 ±0.74	**96.60** ±0.32	**97.53** ±0.63	**97.81** ±0.44	98.18 ±0.51	98.27 ±0.34	98.36 ±0.38	**98.54** ±0.20

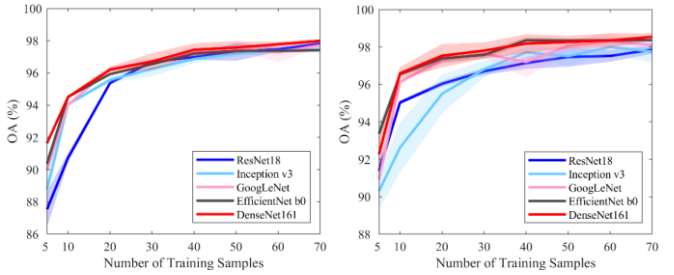

(a) SUP dataset (b) OP dataset

Fig. 6. Comparison of the OA (%) of fine-tuning stage 2 versus the number of training samples on: (a) SUP dataset, (b) OP dataset.

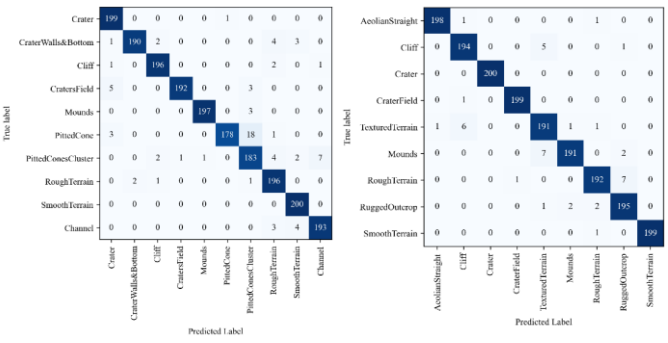

(a) SUP (b) OP

Fig. 7. Confusion matrices of the proposed SDFT approach when the number of training sample is 20 on (a) SUP dataset (OA: 96.20%) and (b) OP dataset (OA: 97.72%).

training samples per class is 21, while the minimum sample size is only 7. Fig. 5 (a2) and (b2) are the reference maps to (a1) and (b1), respectively, which were manually labeled to validate the accuracy of the classification map.

C. Quantitative Results

1) Quantitative results of stepwise transfer

To evaluate the performance of stepwise transfer, five popular feature extraction networks (*i.e.*, GoogLeNet, EfficientNet_b0, ResNet18, Inception_v3, and DenseNet161) were compared. The networks were selected based on their excellent overall classification performance. For example, DenseNet161 exhibited superior classification performance compared to other state-of-the-art CNN networks in [39] and [40]. ResNet18 is a lightweight network that is frequently employed in few-shot classification tasks [48, 49]. The overall accuracy (OA) of the fine-tuning stages 1 and fine-tuning stage 2 are provided in TABLE III, TABLE IV and TABLE V. The pre-training parameters of the models are fine-tuned at each transfer stage.

Fine-tuning stage 1 (ImageNet to DoMars16k): TABLE III provides the accuracy comparison of different feature extractors for fine-tuning stage 1. The average OA and the related standard deviation (SD) on five runs are also given. One can observe that the DenseNet161 feature extractor achieved the highest mean accuracy and the lowest standard deviation.

Fine-tuning stage 2 (DoMars16k to SUP/OP): TABLE IV and TABLE V present the average OA and SD values with different sample sizes (*i.e.*, 5, 10, 20, 30, 40, 50, 60, and 70 samples) for the fine-tuning stage 2 on the SUP and OP datasets, respectively. Furthermore, the data from TABLE IV and TABLE V are plotted in Fig. 6 (a) and (b), respectively, which depicts the mean OA value and the associated SD value for each curve.

As shown in Fig. 6 (a), the accuracy gradually increased by increasing the sample size, stabilizing with 30 training samples. The accuracy of each feature extractor remained relatively consistent when the number of training samples exceeded 30. Overall, the DenseNet161 demonstrated superior performance compared to other models, especially in cases involving very small sample sizes (*e.g.*, 5 and 20). Thus, the DenseNet161 was employed for the subsequent landform mapping.

TABLE V provides the average OA and SD values versus the numbers of samples in the fine-tuning stage 2 on the OP dataset. The same conclusions can be drawn with regard to the SUP dataset. As illustrated in Fig. 6 (b), the accuracy showed a gradual increase by an increasing the sample size, and reached saturation with 20 training samples. Both the DenseNet161 and EfficientNet_b0 demonstrated high accuracy and outperformed other models in cases where various numbers of samples were used. The SD values of EfficientNet_b0 were typically lower than those of DenseNet161, indicating that EfficientNet_b0 exhibited greater robustness than DenseNet161. However, when accuracy was compared with a small number of samples (*e.g.*, 10 and 20), DenseNet161 demonstrated superior performance to EfficientNet_b0.

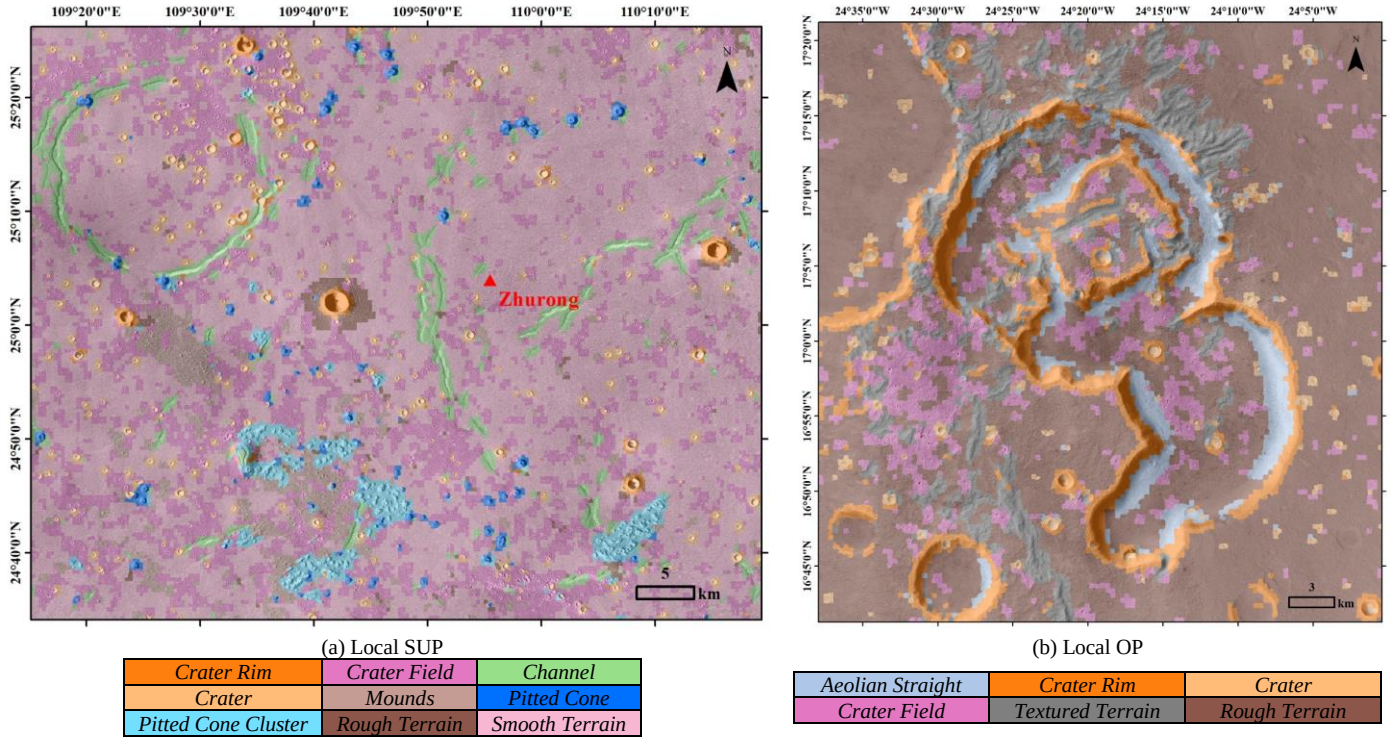

Fig. 8. Mapping results of the proposed SDFT approach on (a) local SUP and (b) local OP.

TABLE VI
OA (%) OBTAINED IN THE ABLATION EXPERIMENTS OF THE PROPOSED SDFT APPROACH ON THE SUP AND THE OP DATASETS WHEN THE NUMBER OF TRAINING SAMPLE IS 20.

Datasets	*No transfer*	*One step transfer*	***Stepwise transfer (Proposed SDFT)***
SUP	81.68 ± 6.71	93.50 ± 0.68	**96.20 ± 0.20**
OP	79.87 ± 2.67	94.97 ± 0.73	**97.53 ± 0.63**

2) Confusion Matrix Analysis

Fig. 7 presents the confusion matrices for the proposed SDFT approach on the SUP and OP datasets when the number of training samples is 20. One can see that in the SUP dataset, the *PittedConesCluster* significantly misclassified in comparison to other classes (*e.g.*, *Pitted Cone*, *Channel*, *Rough Terrain*, *Crater Field*, *Mounds*). In particular, there were misclassification of 18 *Pitted Cone* samples as *Pitted Cones Cluster*. The considerable disparity between the crater wall and the crater floor allows for a variety of potential landform configurations. Therefore, *Crater Wall&Bottom* was misclassified as *Rough Terrain*, *Smooth Terrain*, *Cliff* and *Crater*. Fig. 7 (b) illustrates the severe misclassification of *Textured Terrain* and *Mounds* into other classes. In particular, *Textured Terrain* was misclassified as *Cliff*, and *Mounds* was misclassified as *TexturedTerrain*. This may due to the fact that *Textured Terrain* consists of both smooth and undulating terrains, which are similar to *Mounds* and *Cliff* in certain instances. In addition, *Rough Terrain* were misclassified into *Rugged Outcrop*.

3) Ablation Experiments

TABLE VI provides the ablation experimental results for the proposed SDFT approach. *No transfer* indicates that the feature extraction layers of DenseNet161 are trained from scratch on the small labeled target samples. *One step transfer* denotes the process of fine-tuning the feature extraction layers of DenseNet161, which were pre-trained on the source data 1 (*i.e.*, ImageNet). In both *No transfer* and *One step transfer* scenarios, source data 2 was not utilized. It is clear that the proposed SDFT yielded the highest accuracies (*i.e.*, 96.20% and 97.53%), outperforming *One step transfer* by an increase of 2.7% and 2.56% on the SUP and OP datasets, respectively. This confirmed the necessity of the Earth-to-Mars feature transition in the FTT step. Meanwhile, *One step transfer* exhibits accuracy improvements of 11.82% and 15.1% relative to *No transfer* on the SUP and OP datasets. The SD of OA values for SDFT were the smallest, confirming its superiority.

D. Mapping Results and Analysis

1) Landform Mapping Results

Fig. 8 shows the maps obtained by the proposed SDFT approach on local SUP and OP regions. One can see that *Crater Field* and *Smooth Terrain* represent the basic landform within the local SUP [Fig. 8 (a)]. Two distinct intermittent *Channels* were identified on either side of the Zhurong landing site. In the northwest corner of the mapping results, the *Channel* exhibited a near-circular shape, which has been interpreted as evidence of "ghost craters" or circular graben [50]. *Pitted Cones* were observed to be distributed throughout the region. The majority of *Pitted Cone Clusters* were mainly located in the southern part of the region. Furthermore, the clustered *Mounds* have been identified in the southern region, in close proximity to the aforementioned "ghost craters" and in the vicinity of the *Pitted Cone Clusters*. In this region, the layered ejecta of the rampart crater was designated as *Rough Terrain*, and the rim of the crater, which exceeds the window size, was classified as *Crater*

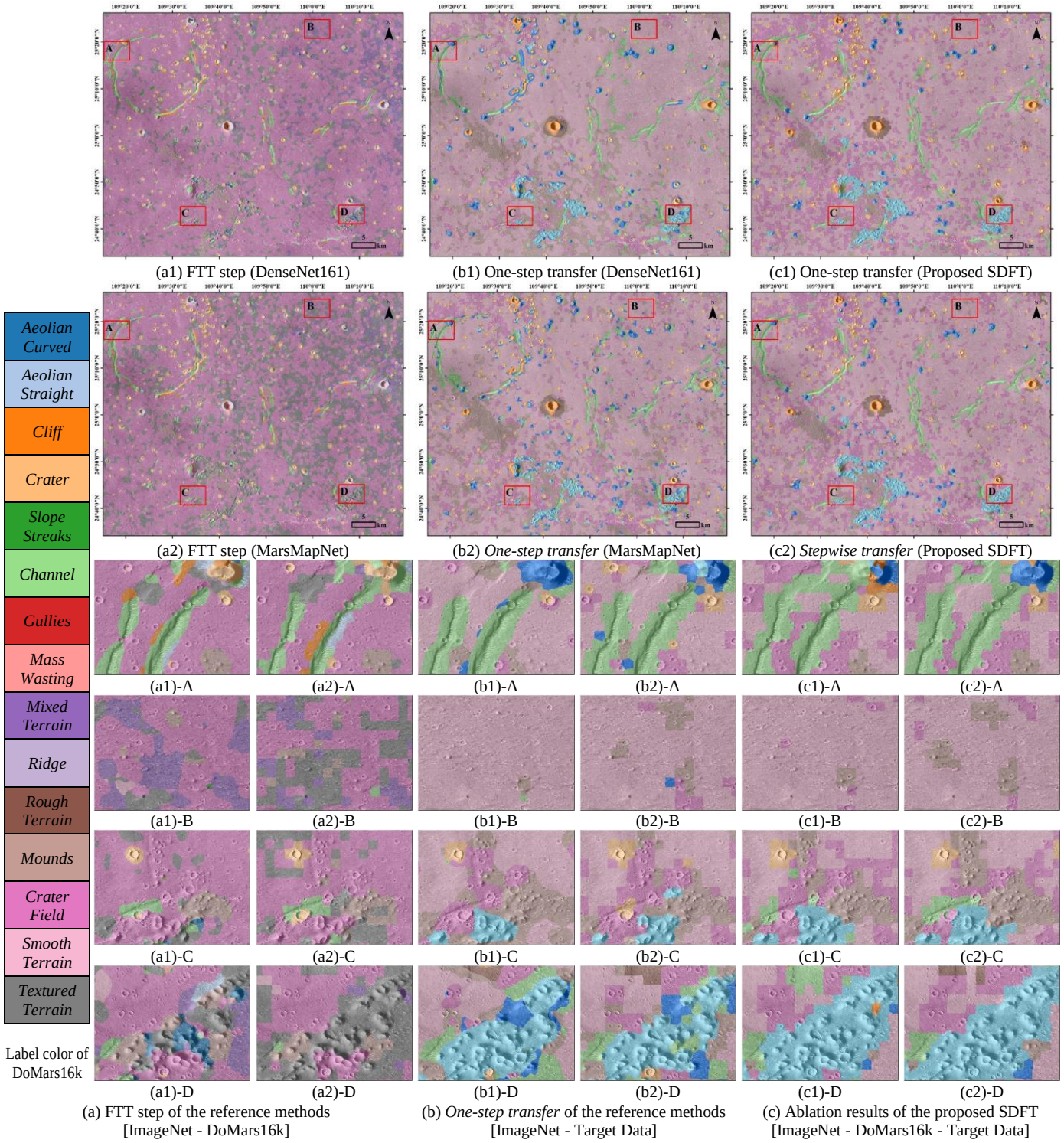

Fig. 9. Mapping results obtained by the reference methods and the proposed SDFT approach on the SUP dataset. The first two columns (a) show the results of the FTT step of the reference methods. The second two columns (b) show the results of the *One-step transfer* of the reference methods. The third two columns (c) show the results of the ablation of the proposed SDFT approach, where (c1) represents the results of the *One-step transfer* of the simplified version of the proposed SDFT approach, and (c2) depicts the results of the proposed SDFT approach.

Rim in our classification system. The *Rough Terrain* around the rampart crater and the *Crater Rim* of the large crater were correctly identified. However, some confusion can be observed on certain classes. For example, there was confusion between *Pitted Cone* and *Pitted Cone Clusters*, *Channel* and *Rough Terrain*, and *Crater Field* and *Pitted Cone Clusters*. In Fig. 8 (b), *Rough Terrain* was identified as the primary basic landform in the local OP, whereas *Crater* and *Crater Field* were found throughout the region. *Crater Rim* could be continuously identified. In the presence of wind, sand particles continue to accumulate at the bottom of the crater, forming *Aeolian Straight.*

2) Comparative Analysis

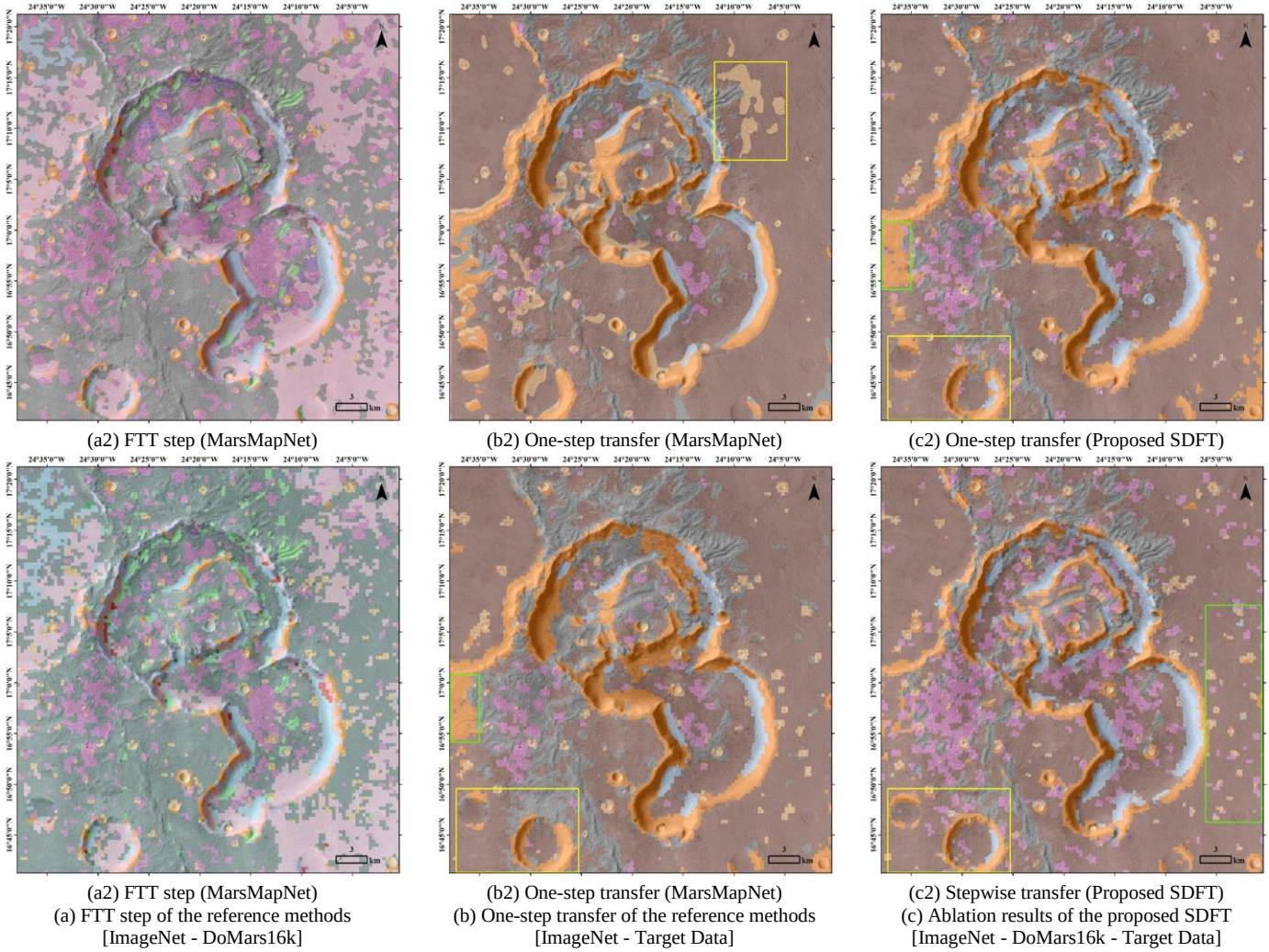

Fig. 10. Mapping results obtained by the reference methods and the proposed SDFT approach on the OP dataset. The first column (a) shows the results of the FTT step of the reference methods; The second column (b) shows the results of the *One-step transfer* of the reference methods; The third column (c) shows the results of the ablation of the proposed SDFT approach, where (c1) represents the results of the *One-step transfer* of the simplified version of the proposed SDFT approach, and (c2) depicts the results of the proposed SDFT approach.

Figs.9 and 10 present the mapping results of the reference methods and the proposed SDFT approach on local SUP and OP, respectively. Two reference methods (*i.e.*, DenseNet161 [39] and MarsMapNet [40]), which represent the state-of-the-art in Martian landform classification, were selected for comparison. In [39], the DenseNet161 network was employed to map Martian landforms based on a pixel-by-pixel sliding-window approach, with Markov random fields (MRFs) being used to mitigate the impact of outliers on the mapping results. In [40], abstract convolutional features extracted from scene-level patches were combined with multi-textures derived from local landforms to enhance classification performance. Meanwhile, a superpixel-guided landform mapping approach was proposed to improve efficiency.

Fig. 9 (a) and Fig. 10 (a) show the mapping results with 15 landform classes of the first FTT step of the reference methods, in which the model pre-trained on the ImageNet dataset was re-trained on the DoMars16k dataset. Fig. 9 (b) and Fig. 10 (b) show the mapping results of the *One-step transfer* of the reference methods, without using the DoMars16k data and by directly fine-tuning the model pre-trained on the ImageNet dataset on Earth on the target samples from local SUP and OP. Fig. 9 (c) and Fig. 10 (c) illustrate the ablation results of the proposed SDFT approach. Fig. 10 (c1) refers to *One-step transfer* of the simplified version of the proposed SDFT approach, where the DoMars16k dataset was not employed and the model that pre-trained on the ImageNet dataset was fine-tuned on the targeted dataset. Fig. 10 (c2) illustrates the results of the proposed SDFT approach. It is noteworthy that the cosine distance classifier was used in the proposed SDFT approach, whereas the linear classifier was utilized in the reference methods.

The obtained maps are qualitatively compared in Fig. 9 (a) and (b). The class system shown in Fig. 9 (a) is derived from the public DoMars16k dataset, which contains a fixed set of 15 classes. The class system depicted in Fig. 9 (b) was customized for the target study area. Since the landforms represented in the DoMars16k dataset do not precisely align with those observed in the local SUP region, the maps in Fig. 9 (a) are less accurate compared to those presented in Fig. 9 (b). Specifically, *Channel* segments with weaker feature were not identified, resulting in poor continuity of the whole *Channel* [see Fig. 9 (a1/a2)-A].

Some classes (*e.g.*, *Mixed Terrain*, *Aeolian Curved* and *Aeolian Straight*) in the DoMars16k dataset were not present in the local SUP area, but were erroneously included in the mapping results [see *Mixed Terrain* in Fig. 9 (a1/a2)-B] and *Aeolian Curved* in Fig. 9 (a1)-C/D]. Some individual *Pitted Cones* in the local SUP area were not included in the DoMars16k dataset, resulting in the misclassification of *Pitted Cones* as *Craters* [see Fig. 9 (a1/a2)-A]. This is due to the fact that they have very similar geometric properties. The *Pitted Cone Cluster* in the local SUP area exhibited a larger size than those in the DoMars16k dataset, resulting in the *Pitted Cone Cluster* being incorrectly classified as a *Crater Field* [see Fig. 9 (a1/a2)-C] and *Textured Terrain* [see Fig. 9 (a1/a2)-D]. The mapping results in Fig. 9 (b1) and (b2) show a notable improvement compared to (a1) and (a2), which can be attributed to the use of customized samples from the local SUP area. Specifically, the *Pitted Cone* was partially recognized [see Fig. 9 (b1/b2)-A], the *Pitted Cone Cluster* [see Fig. 9 (b1)-C/D and (b2)-C/D] and *Mounds* [see Fig. 9 (b1)-C and (b2)-B/C] were correctly identified. However, the maps shown in Fig. 9 (b1) and (b2) remained inadequate. For example, the continuity of the *Channel* was not accurate, and the *Smooth Terrain* in Fig. 9 (b2)-A/B/D was misclassified as *Pitted Cone*.

TABLE VII
COMPARISON OF THE CLASSIFICATION ACCURACIES (%) PROVIDED BY DIFFERENT METHODS ON THE TWO CONSIDERED STUDY AREAS.

		Reference methods (One-step transfer)		**Proposed SDFT (Ablation comparison)**	
		DenseNet161	MarsMapNet	*One-step transfer*	*Stepwise transfer*
Local SUP	OA	65.93	72.12	84.56	**93.90**
	AA	74.67	74.14	83.08	**92.00**
	Kappa	59.70	66.30	80.78	**92.40**
	mIoU	54.77	54.36	69.95	**86.13**
Local OP	OA	71.78	77.79	80.24	**90.82**
	AA	62.75	71.98	72.72	**90.07**
	Kappa	63.95	71.46	74.72	**88.39**
	mIoU	48.73	59.82	61.52	**82.04**

A further comparison of the two reference methods, as illustrated in Fig. 9 (a) and (b), respectively, reveals that the landform boundary in Fig. 9 (a1) and (b1) (*i.e.*, DenseNet161) is smoother than those in Fig. 9 (a2) and (b2) (*i.e.*, MarsMapNet). However, benefiting from the superpixel-guided technique, the time consumption required by the MarsMapNet approach was significantly reduced when comparing to DenseNet161. Moreover, the boundary adhesion performance was very poor, as evidenced in Fig. 9 (a2) and (b2). In addition, the use of local-scale multi-texture features enables the MarsMapNet to properly recognize small-scale landforms. For example, more craters were recognized in Fig. 9 (b2)-A/C, and almost all of the sporadic and small mounds in Fig. 9 (b2)-B were correctly recognized when compared to the corresponding localized map in Fig. 9 (b1).

Fig. 9 (c2) depicts the maps predicted by the proposed SDFT approach. It can be observed that the *Channel* exhibited enhanced continuity [see Fig. 9 (c2)-A], and the *Pitted Cone* was successfully recognized in its entirety [see Fig. 9 (c2)-A], both the sporadic and clustered *Mounds* were well identified [see Fig. 9 (c2)-B/C], and the *Pitted Cone Cluster* was completely detected [see Fig. 9 (c2)-C/D]. Compared to Fig. 9 (c2), the intermediate step transfer was not used for the results in Fig. 9 (c1), introducing worse accuracy. For example, both the *Pitted Cone* [see Fig. 9 (c1)-A] and the sporadic *Mounds* [see in Fig. 9 (c1)-B] were only partially identified, while the *Smooth Terrain* in Fig. 9 (c1)-C/D was partially misclassified as *Channel*. The necessity of the stepwise transfer was further validated by the ablation experiments.

Fig. 10 (a1) and (a2) exhibit messy mapping results, with the rim of impact crater being divided into multiple sections: *Cliff*, *Ridge* and *Textured Terrain*, while the rough terrain situated in the upper left region was misclassified as *Aeolian Straight*. The customization of the landform system to the region, resulted in the significantly more accurate results of Fig. 10 (b1) and (b2). In particular, both the *Crater Rim* and the *Aeolian Straight* near the bottom of the *Crater Rim* were fully discernible. In Fig. 10 (b1), the *Rough Terrain* was incorrectly classified as *Crater* (highlighted in yellow rectangle), whereas in Fig. 10 (b2) it was correctly identified. However, the mapping results in Fig. 10 (b2) were still inadequate, as the *Crater Rim* was erroneously located on the left side of the region [see green rectangle in Fig. 10 (b2)] and the *Crater Rim* was not sufficiently continuous [see the yellow rectangle in Fig. 10 (b2)]. Fig. 10 (c2) exhibits the best visual mapping result, which was obtained by the proposed SDFT method. In Fig. 10 (c2), the continuous and complete *Crater Rim* was clearly delineated [see the yellow rectangle in Fig. 10 (c2)], and the *Crater* and *Crater Field* with weak features were also correctly recognized [see the green rectangle in Fig. 10 (c2)]. The lack of an intermediate transfer step resulted in the inferior classification results shown in Fig. 10 (c1). For example, there was a wrong *Crater Rim* in the green rectangle, and the continuity of the *Crater Rim* in the yellow rectangle was less satisfactory in Fig. 10 (c1).

To provide a further quantitative evaluation of the accuracy of the classification maps produced by the proposed method, as well as of those produced by the comparison techniques, the OA, average accuracy (AA), Kappa coefficient (Kappa), mean Intersection-over-Union (mIoU) were calculated and presented in TABLE VII, based on Fig. 5 (a2) and (b2). A comparison of the reference methods revealed that MarsMapNet achieved 6.19% and 6.01% higher OA than DenseNet161 on Local SUP and Local OP datasets, respectively. Although the MarsMapNet exhibited a marginal 0.41% lower mIoU than the DenseNet161 on the Local SUP, it achieved a substantial 11.09% higher mIoU on the Local OP. The proposed SDFT (*i.e.*, stepwise transfer) achieved the highest accuracies among all reference methods. Also, it outperformed the one-step transfer of the proposed SDFT method, demonstrating the necessity of the two-step transfer. Moreover, the stepwise transfer of the proposed SDFT method significantly improved the reference methods. The one-step transfer of the proposed SDFT also outperformed the reference methods, confirming the advantage of the cosine distance classifier used by the proposed method over the linear classifier used by the reference methods, particularly when using a small number of labeled samples.

IV. Conclusions

In this paper, we have proposed a novel SDFT model for Martian landform mapping, in order to address the challenges of time-consuming and labeling an adequate number of samples especially in a specific local target region. The two transfer steps (i.e., FTT and FAT steps) in the proposed SDFT model mitigate the challenges associated with different datasets. In particular, in the FTT step, the standard pre-training and fine-tuning procedure is employed to transfer the large dataset from Earth to the medium-sized dataset from Mars. This enables the transition of data and classes between Earth and Mars. The model obtained in the FTT step is further transferred to the small sample dataset in the FAT step. Intra-class variations in the features of the small samples are reduced by a distance-based classifier, thus facilitating more accurate classifications.

In our experiments, the quantitative analysis and qualitative mapping analysis were conducted on two study areas (i.e., SUP and OP regions) with mosaic CTX image. In quantitative analysis experiments, the classification accuracies analysis with different feature extractors and training sample sizes, and the ablation experiment analysis demonstrated the effectiveness of the proposed SDFT model. In qualitative mapping analysis experiments, the landform mapping was performed in local SUP and OP regions with no more than 21 samples per class, and the obtained maps confirmed the superiority of the proposed method in comparison to existing state-of-the-art techniques. In future work, we plan to investigate the potential of the proposed model for transferring across different resolutions and source data on Mars and other planets.

Acknowledgments

We thank the scientists and engineers who built the CTX mosaic data (http://murraylab.caltech.edu/CTX/), and the authors of paper [34] for providing the DoMars16k dataset, and the MOLA team for providing the MOLA DEM product (https://astrogeology.usgs.gov/search/map/Mars/GlobalSurveyor/MOLA/Mars_MGS_MOLA_DEM_mosaic_global_463m).

References

[1] H. Zeng, S. Liu, Z. Zhang, X. Liu, X. Tong, H. Xie, K. Du, and J. Zhang, "A Novel Cross-Instrument Spectral Harmonization Approach for Mars In Situ LIBS Data," *IEEE Transactions on Geoscience and Remote Sensing*, vol. 62, pp. 1-11, 2024.

[2] S. Liu, Y. Lin, K. Du, J. Zhang, X. Tong, H. Xie, B. Wan, and Z. Zhang, "A Novel In Situ Dust Cover Index for Analyzing the Multispectral Camera Image Acquired by China's Zhurong Mars Rover," *IEEE Transactions on Geoscience and Remote Sensing*, vol. 63, pp. 1-13, 2025.

[3] S. Liu, Z. Zhang, J. Zhang, K. Du, X. Tong, H. Xie, Y. Feng, and Y. Jin, "LIBSFormer: Enhancing Mars in-situ LIBS data analysis with accurate and interpretable quantification of oxides," *Spectrochimica Acta Part B: Atomic Spectroscopy*, vol. 229, 2025.

[4] D. E. Smith, M. T. Zuber, H. V. Frey, J. B. Garvin, J. W. Head, D. O. Muhleman, G. H. Pettengill, R. J. Phillips, S. C. Solomon, H. J. Zwally, W. B. Banerdt, T. C. Duxbury, M. P. Golombek, F. G. Lemoine, G. A. Neumann, D. D. Rowlands, O. Aharonson, P. G. Ford, A. B. Ivanov, C. L. Johnson, P. J. McGovern, J. B. Abshire, R. S. Afzal, and X. Sun, "Mars Orbiter Laser Altimeter: Experiment summary after the first year of global mapping of Mars," *Journal of Geophysical Research: Planets*, vol. 106, no. E10, pp. 23689-23722, 2001.

[5] P. R. Christensen, B. Jakosky, H. H. Kieffer, M. C. Malin, H. Y. McSween, K. Nealson, G. L. Mehall, S. H. Silverman, S. Ferry, M. Caplinger, and M. Ravine, "The Thermal Emission Imaging System (THEMIS) for the Mars 2001 Odyssey Mission," *Space Science Reviews*, vol. 110, pp. 85-130, 2004.

[6] M. C. Malin, J. F. Bell, B. A. Cantor, M. A. Caplinger, W. M. Calvin, R. T. Clancy, K. S. Edgett, L. Edwards, R. M. Haberle, P. B. James, S. W. Lee, M. A. Ravine, P. C. Thomas, and M. J. Wolff, "Context Camera Investigation on board the Mars Reconnaissance Orbiter," *Journal of Geophysical Research: Planets*, vol. 112, no. E5, pp. 1-25, 2007.

[7] A. S. McEwen, E. M. Eliason, J. W. Bergstrom, N. T. Bridges, C. J. Hansen, W. A. Delamere, J. A. Grant, V. C. Gulick, K. E. Herkenhoff, L. Keszthelyi, R. L. Kirk, M. T. Mellon, S. W. Squyres, N. Thomas, and C. M. Weitz, "Mars Reconnaissance Orbiter's High Resolution Imaging Science Experiment (HiRISE)," *Journal of Geophysical Research: Planets*, vol. 112, no. E5, pp. 1-40, 2007.

[8] Q. Meng, D. Wang, X. Wang, W. Li, X. Yang, D. Yan, Y. Li, Z. Cao, Q. Ji, T. Sun, W. Yan, K. Wang, X. Li, J. Huang, Z. Wang, W. Zhao, Y. Wang, Y. He, X. Hao, W. Liu, B. Zhang, P. Zhou, Y. Li, H. Zhao, L. Lu, H. Guan, D. Zhou, F. Wu, F. Zhang, S. Zhu, and J. Dong, "High Resolution Imaging Camera (HiRIC) on China's First Mars Exploration Tianwen-1 Mission," *Space Science Reviews*, vol. 217, pp. 1-29, 2021.

[9] P. Kumari, S. Soor, A. Shetty, and S. G. Koolagudi, "Mineral classification on Martian surface using CRISM hyperspectral data: a survey," *Journal of Applied Remote Sensing*, vol. 17, no. 4, pp. 041501.1-041501.31, 2023.

[10] M. A. Ivanov, H. Hiesinger, G. Erkeling, and D. Reiss, "Mud volcanism and morphology of impact craters in Utopia Planitia on Mars: Evidence for the ancient ocean," *Icarus*, vol. 228, pp. 121-140, 2014.

[11] N. H. Warner, A. J. Schuyler, A. D. Rogers, M. P. Golombek, J. Grant, S. Wilson, C. Weitz, N. Williams, and F. Calef, "Crater Morphometry on the Mafic Floor Unit at Jezero Crater, Mars: Comparisons to a Known Basaltic Lava Plain at the InSight Landing Site," *Geophysical Research Letters*, vol. 47, no. 17, pp. e2020GL089607, 2020.

[12] M. P. Golombek, N. H. Warner, V. Ganti, M. P. Lamb, T. J. Parker, R. L. Fergason, and R. Sullivan, "Small crater modification on Meridiani Planum and implications for erosion rates and climate change on Mars," *Journal of Geophysical Research: Planets*, vol. 119, no. 12, pp. 2522-2547, 2014.

[13] M. Ono, B. Rothrock, E. Almeida, A. Ansar, R. Otero, A. Huertas, and M. Heverly, "Data-Driven Surface Traversability Analysis for Mars 2020 Landing Site Selection," *2016 Ieee Aerospace Conference*, 2016.

[14] J. A. Grant, M. P. Golombek, S. A. Wilson, K. A. Farley, K. H. Williford, and A. Chen, "The science process for selecting the landing site for the 2020 Mars rover," *Planetary and Space Science*, vol. 164, pp. 106-126, 2018.

[15] S. J. Robbins and B. M. Hynek, "A new global database of Mars impact craters ⩾1 km: 2. Global crater properties and regional variations of the simple - to - complex transition diameter," *Journal of Geophysical Research: Planets*, vol. 117, no. E6, pp. 1-21, 2012.

[16] S. J. Robbins and B. M. Hynek, "A new global database of Mars impact craters ⩾1 km: 1. Database creation, properties, and parameters," *Journal of Geophysical Research: Planets*, vol. 117, no. E5, pp. 1-18, 2012.

[17] M. E. Schwamb, K.-M. Aye, G. Portyankina, C. J. Hansen, C. Allen, S. Allen, F. J. Calef, S. Duca, A. McMaster, and G. R. M. Miller, "Planet Four: Terrains - Discovery of araneiforms outside of the South Polar layered deposits," *Icarus*, vol. 308, pp. 148-187, 2018.

[18] K. M. Aye, M. E. Schwamb, G. Portyankina, C. J. Hansen, A. McMaster, G. R. M. Miller, B. Carstensen, C. Snyder, M. Parrish, S. Lynn, C. Mai, D. Miller, R. J. Simpson, and A. M. Smith, "Planet Four: Probing springtime winds on Mars by mapping the southern polar CO2 jet deposits," *Icarus*, vol. 319, pp. 558-598, 2019.

[19] L. K. Fenton, "Updating the global inventory of dune fields on Mars and identification of many small dune fields," *Icarus*, vol. 352, pp. 114018, 2020.

[20] M. M. Mills, A. S. McEwen, and C. H. Okubo, "A Preliminary Regional Geomorphologic Map in Utopia Planitia of the Tianwen - 1 Zhurong Landing Region," Geophysical Research Letters, vol. 48, no. 18, 2021.

[21] T. Stepinski and R. Vilalta, "Digital Topography Models for Martian Surfaces," *IEEE Geoscience and Remote Sensing Letters*, vol. 2, no. 3, pp. 260-264, 2005.

[22] B. D. Bue and T. F. Stepinski, "Automated classification of landforms on Mars," Computers & Geosciences, vol. 32, no. 5, pp. 604-614, 2006.

[23] T. F. Stepinski and C. Bagaria, "Segmentation-Based Unsupervised Terrain Classification for Generation of Physiographic Maps," *IEEE Geoscience and Remote Sensing Letters*, vol. 6, no. 4, pp. 733-737, 2009.

[24] D. Miao, J. Yan, Z. Tu, and J.-P. Barriot, "LCDNet: An Innovative Neural Network for Enhanced Lunar Crater Detection Using DEM Data," *IEEE Journal of Selected Topics in Applied Earth Observations and Remote Sensing*, vol. 17, pp. 11034-11049, 2024.

[25] F. Zhang, Z. Tu, W. Hao, Y. Chen, F. Li, and M. Ye, "Zero-Shot Parameter Learning Network for Low-Light Image Enhancement in Permanently Shadowed Regions," *IEEE Transactions on Geoscience and Remote Sensing*, vol. 62, pp. 1-16, 2024.

[26] L. Bandeira, J. S. Marques, J. Saraiva, and P. Pina, "Automated Detection of Martian Dune Fields," *IEEE Geoscience and Remote Sensing Letters*, vol. 8, no. 4, pp. 626-630, 2011.

[27] L. Bandeira, J. S. Marques, J. Saraiva, and P. Pina, "Advances in automated detection of sand dunes on Mars," *Earth Surface Processes and Landforms*, vol. 38, no. 3, pp. 275-283, 2013.

[28] D. Carrera, L. Bandeira, R. Santana, and J. A. Lozano, "Detection of sand dunes on Mars using a regular vine-based classification approach," *Knowledge-Based Systems*, vol. 163, pp. 858-874, 2019.

[29] Y. Wang, K. Di, X. Xin, and W. Wan, "Automatic detection of Martian dark slope streaks by machine learning using HiRISE images," *Isprs Journal of Photogrammetry and Remote Sensing*, vol. 129, pp. 12-20, 2017.

[30] T. Statella, P. Pina, and E. A. da Silva, "Image processing algorithm for the identification of Martian dust devil tracks in MOC and HiRISE images," *Planetary and Space Science*, vol. 70, no. 1, pp. 46-58, 2012.

[31] W. Li, K. Di, Z. Yue, Y. Liu, and S. Sun, "Automated Detection of Martian Gullies from HiRISE Imagery," *Photogrammetric Engineering & Remote Sensing*, vol. 81, no. 12, pp. 913-920, 2015.

[32] J. Zhang, S. Liu, K. Du, X. Tong, H. Xie, Y. Feng, Y. Jin, Y. Lin, and B. Wan, "Automatic extraction of Transverse Aeolian Ridges (TARs) and analysis of landform influence for the Zhurong landing area on Mars," *Geomorphology*, vol. 467, 2024.

[33] B. Rothrock, R. Kennedy, C. Cunningham, J. Papon, M. Heverly, and M. Ono, "SPOC: Deep Learning-based Terrain Classification for Mars Rover Missions," *Aiaa Space 2016*, 2016.

[34] M. Ono, M. Heverly, B. Rothrock, E. Almeida, F. Calef, T. Soliman, N. Williams, H. Gengl, T. Ishimatsu, A. Nicholas, E. Stilley, K. Otsu, R. Lange, and S. M. Milkovich, "Mars 2020 Site-Specific Mission Performance Analysis: Part 2. Surface Traversability," *2018 AIAA SPACE and Astronautics Forum and Exposition*, 2018.

[35] A. M. Barrett, M. R. Balme, M. Woods, S. Karachalios, D. Petrocelli, L. Joudrier, and E. Sefton-Nash, "NOAH-H, a deep-learning, terrain classification system for Mars: Results for the ExoMars Rover candidate landing sites," *Icarus*, vol. 371, pp. 114701, 2022.

[36] J. Li, L. Zhang, Z. Wu, Z. Ling, X. Cao, K. Guo, and F. Yan, "Autonomous Martian rock image classification based on transfer deep learning methods," *Earth Science Informatics*, vol. 13, no. 3, pp. 951-963, 2020.

[37] K. L. Wagstaff, Y. Lu, A. Stanboli, K. Grimes, T. Gowda, and J. Padams, "Deep Mars: CNN Classification of Mars Imagery for the PDS Imaging Atlas," *Thirty-Second Aaai Conference on Artificial Intelligence / Thirtieth Innovative Applications of Artificial Intelligence Conference / Eighth Aaai Symposium on Educational Advances in Artificial Intelligence*, pp. 7867-7872, 2018.

[38] K. Wagstaff, S. Lu, E. Dunkel, K. Grimes, B. Zhao, J. Cai, S. B. Cole, G. Doran, R. Francis, J. Lee, and L. Mandrake, "Mars Image Content Classification: Three Years of NASA Deployment and Recent Advances," *Thirty-Fifth Aaai Conference on Artificial Intelligence, Thirty-Third Conference on Innovative Applications of ArtificialIntelligence and the Eleventh Symposium on Educational Advances in Artificial Intelligence*, vol. 35, pp. 15204-15213, 2021.

[39] T. Wilhelm, M. Geis, J. Püttschneider, T. Sievernich, T. Weber, K. Wohlfarth, and C. Wöhler, "DoMars16k: A Diverse Dataset for Weakly Supervised Geomorphologic Analysis on Mars," *Remote Sensing*, vol. 12, no. 23, pp. 3981, 2020.

[40] H. Zhao, S. Liu, X. Tong, Q. Du, L. Bruzzone, K. Du, J. Zhang, and X. Lu, "MarsMapNet: A Novel Superpixel-Guided Multiview Feature Fusion Network for Efficient Martian Landform Mapping," *IEEE Transactions on Geoscience and Remote Sensing*, vol. 62, pp. 1-16, 2024.

[41] J. Deng, W. Dong, R. Socher, L. J. Li, K. Li, and F. F. Li, "ImageNet: A Large-Scale Hierarchical Image Database," *Cvpr: 2009 Ieee Conference on Computer Vision and Pattern Recognition*, vol. 1-4, pp. 248-255, 2009.

[42] T. Mensink, J. Verbeek, F. Perronnin, and G. Csurka, "Metric Learning for Large Scale Image Classification: Generalizing to New Classes at Near-Zero Cost," *Computer Vision - Eccv 2012, Pt Ii*, vol. 7573, pp. 488-501, 2012.

[43] S. Gidaris and N. Komodakis, "Dynamic Few-Shot Visual Learning without Forgetting," *2018 Ieee/Cvf Conference on Computer Vision and Pattern Recognition (Cvpr)*, pp. 4367-4375, 2018.

[44] R. Achanta, A. Shaji, K. Smith, A. Lucchi, P. Fua, and S. Susstrunk, "SLIC superpixels compared to state-of-the-art superpixel methods," *IEEE Trans Pattern Anal Mach Intell*, vol. 34, no. 11, pp. 2274-2282, 2012.

[45] Wei-Yu Chen, Yen-Cheng Liu, Zsolt Kira, Yu-Chiang Frank Wang, and J.-B. Huang, "A closer look at few-shot classification," arXiv:1904.04232, 2020.

[46] W. Li, Z. Wang, X. Yang, C. Dong, P. Tian, T. Qin, J. Huo, Y. Shi, L. Wang, Y. Gao, and J. Luo, "LibFewShot: A Comprehensive Library for Few-Shot Learning," *IEEE Transactions on Pattern Analysis and Machine Intelligence*, vol. 45, no. 12, pp. 14938-14955, 2023.

[47] George E. McGill, "Buried topography of Utopia, Mars: Persistence of a giant impact depression," *Journal of Geophysical Research: Solid Earth*, vol. 94, no. B3, pp. 2753-2759, 1989.

[48] K. L. Tanaka, S. J. Robbins, C. M. Fortezzo, J. A. Skinner, and T. M. Hare, "The digital global geologic map of Mars: Chronostratigraphic ages, topographic and crater morphologic characteristics, and updated resurfacing history," *Planetary and Space Science*, vol. 95, pp. 11-24, 2014.

[49] C. Quantin-Nataf, J. Carter, L. Mandon, P. Thollot, M. Balme, M. Volat, L. Pan, D. Loizeau, C. Millot, S. Breton, E. Dehouck, P. Fawdon, S. Gupta, J. Davis, P. M. Grindrod, A. Pacifici, B. Bultel, P. Allemand, A. Ody, L. Lozach, and J. Broyer, "Oxia Planum: The Landing Site for the ExoMars "Rosalind Franklin" Rover Mission: Geological Context and Prelanding Interpretation," *Astrobiology*, vol. 21, no. 3, pp. 345-366, Mar 2021.

[50] B. Ye, Y. Qian, L. Xiao, J. R. Michalski, Y. Li, B. Wu, and L. Qiao, "Geomorphologic exploration targets at the Zhurong landing site in the southern Utopia Planitia of Mars," *Earth and Planetary Science Letters*, vol. 576, pp. 117199, 2021.